Self-similarity of solitary waves on inertia-dominated falling liquid films

Fabian Denner,[1,*] Marc Pradas,[2,3] Alexandros Charogiannis,[3] Christos N. Markides,[3]
Berend G. M. van Wachem,[1] and Serafim Kalliadasis[3]
[1]*Department of Mechanical Engineering, Imperial College London, London SW7 2AZ, United Kingdom*
[2]*Department of Mathematics and Statistics, The Open University, Milton Keynes MK7 6AA, United Kingdom*
[3]*Department of Chemical Engineering, Imperial College London, London SW7 2AZ, United Kingdom*
(Received 28 October 2015; published 21 March 2016)

We propose consistent scaling of solitary waves on inertia-dominated falling liquid films, which accurately accounts for the driving physical mechanisms and leads to a self-similar characterization of solitary waves. Direct numerical simulations of the entire two-phase system are conducted using a state-of-the-art finite volume framework for interfacial flows in an open domain that was previously validated against experimental film-flow data with excellent agreement. We present a detailed analysis of the wave shape and the dispersion of solitary waves on 34 different water films with Reynolds numbers $\mathrm{Re} = 20$–120 and surface tension coefficients $\sigma = 0.0512$–$0.072\ \mathrm{N\,m^{-1}}$ on substrates with inclination angles $\beta = 19^\circ$–90°. Following a detailed analysis of these cases we formulate a consistent characterization of the shape and dispersion of solitary waves, based on a newly proposed scaling derived from the Nusselt flat film solution, that unveils a self-similarity as well as the driving mechanism of solitary waves on gravity-driven liquid films. Our results demonstrate that the shape of solitary waves, i.e., height and asymmetry of the wave, is predominantly influenced by the balance of inertia and surface tension. Furthermore, we find that the dispersion of solitary waves on the inertia-dominated falling liquid films considered in this study is governed by nonlinear effects and only driven by inertia, with surface tension and gravity having a negligible influence.

DOI: 10.1103/PhysRevE.93.033121

I. INTRODUCTION

Falling liquid films have been an active research topic for several decades, starting with the pioneering experiments by the father-son team of the Kapitza family [1,2], and extending to more recent work in both planar [3–6] and annular flow geometries [7,8]. A falling liquid film is an open-flow hydrodynamic system that is convectively unstable to long-wave disturbances at small flow rates. It can be studied with the simplest experimental apparatus (e.g., [6]) while at the same time the theoretical analysis of a falling liquid film is facilitated by the substantial reduction of the complexity of the governing equations offered by the long-wave nature of the instability. The simplicity of the resulting model equations, single evolution equations or coupled averaged evolution equations, makes them useful prototypes for mathematical and numerical scrutiny. Yet, it yields a rich variety of spatial and temporal structures and a rich spectrum of wave forms and wave transitions that are generic to a large class of open-flow hydrodynamic and other nonlinear systems: a unique and experimentally well-characterized sequence of nonlinear secondary transitions that begins with a selected monochromatic disturbance and leads eventually to nonstationary and broad-banded (in both frequency and wave number) "turbulent" wave dynamics, a state of disorder or spatiotemporal chaos. At this stage, despite the apparent complexity one can still identify solitary waves in what appears to be a randomly disturbed surface. It is then essential that in order to understand the spatiotemporal evolution of the film, we fully understand the properties of individual solitary waves which in turn can help us understand the way they interact with each other. In fact, these coherent structures are truly elementary processes so that (by using techniques from nonlinear dynamics and dynamical systems theory) the dynamics of the film can be described by their superposition [9–14]. As a matter of fact the evolution of the film appears to be the result of interaction between solitarylike coherent structures which are stable and robust and interact indefinitely with each other as "quasiparticles." Hence, the falling liquid film can serve as a canonical reference system for the study of weak or dissipative turbulence. This is further facilitated by the substantial reduction of the complexity of the governing equations offered by the long-wave nature of the instability. Also, due to their typically small flow rates and low pressure drops, their large contact area, and their excellent heat and mass transport characteristics [15,16], falling films are utilized in a wide spectrum of engineering and technological applications, such as evaporators, heat exchangers, or chemical reactor columns to name but a few.

Applying a periodic forcing at the inlet with a sufficiently large amplitude, for instance by periodically changing the flow rate of the liquid film, interfacial waves form as a result of the long-wave instability mechanism [17,18] and synchronize with the forcing frequency [19,20]. Depending on the frequency of the forcing, two wave families can be distinguished [19,21]: γ_1 waves and γ_2 waves. The γ_1 waves have a speed smaller than the corresponding spatially amplified infinitesimal wave at the same frequency and are observed close to the inlet at high forcing frequency, close but below the cut-off frequency above which the film is stable. At low forcing frequency, the exponential growth of the waves is followed by the formation of fast solitary waves of γ_2 type. These solitary waves have a dominant elevation with a long tail and steep front, typically with capillary ripples preceding the main wave hump. The γ_1 and γ_2 waves are also observed in falling films in the presence of various complexities, such

*f.denner09@imperial.ac.uk

as Marangoni effects due to heating, localized or uniform [22–26], chemical reactions [27–29], surfactants [30], and substrate curvature [31–35].

In inertia-dominated film flows, solitary waves exhibit a separation of scales between the front of the main wave hump, where gravity, viscous drag, and surface tension balance, and the tail of the wave, characterized by a balance between gravity, viscous drag, and inertia [21]. This leads to a strongly nonparabolic velocity profile at the front of the solitary wave [6,36,37], including flow reversal underneath the trough preceding the solitary wave under certain conditions [4,5,38,39]. Furthermore, if inertia is sufficiently high, the maximum flow velocity of the film exceeds the phase velocity of the solitary waves, leading to a recirculation zone in the main wave hump with respect to the reference frame moving with the wave [39–42]. This flow recirculation was found to have a considerable impact on the heat and mass transport in the film due to the increased mixing [15,42,43].

The long-wave instability mechanism drives the initially exponential growth of the primary instability which via a secondary modulation instability leads to solitary waves [17,18], yet it has a stabilizing effect after the onset of flow recirculation in the main solitary wave hump as was shown recently by Denner *et al.* [37]. As far as the saturated ("equilibrium") height of a solitary wave is concerned, it is governed by a balance of inertia and the streamwise component of gravity (destabilizing), with surface tension, viscous dissipation, and the cross-stream component of gravity (stabilizing). In the limit of zero wave number (i.e., for single isolated waves with infinite wavelength), the phase velocity of solitary waves on an inertia-dominated liquid film is only dependent on the Froude number $\mathrm{Fr} = \sqrt{3\,\mathrm{Re}/\cot\beta}$ [44], where Re is the Reynolds number (defined in Sec. III) and β is the inclination angle of the substrate. However, the dispersion of solitary waves with finite wave number (i.e., waves with finite wavelength and potentially interacting with each other) is more complex and previous studies have focused on the relationship between the phase velocity and the wave height (e.g., [3,20]) or between the phase velocity and the wave number (e.g., [45,46]) of the solitary wave, rather than on the governing physical mechanisms. As a result of the considerable number of parameters dictating the dynamics and evolution of solitary waves, a consistent hydrodynamic characterization that is able to quantify and predict the shape and phase velocity of solitary waves and explain the driving mechanisms of solitary waves, including the influence of flow rate and inclination angle, is not available at present.

Here we present a detailed, systematic, and rational study of the driving mechanisms and detailed characterization of solitary waves on inertia-dominated liquid films on inclined substrates, based on direct numerical simulations (DNSs) that resolve all relevant length and time scales of the full two-phase system using a state-of-the-art finite volume framework for interfacial flows. In a previous study on the dynamics of solitary waves on inertia-dominated falling liquid film of Denner *et al.* [37], the results obtained with the DNS framework [47–49] used in this study showed excellent agreement with experimental measurements [6]. We propose a scaling for solitary waves, which we derive from the Nusselt flat film solution based on the physical mechanisms that underpin the growth and dispersion of solitary waves. Our results demonstrate that the proposed scaling leads to a (surprising) self-similar characterization of solitary waves on liquid films with respect to the proposed nondimensional numbers and the inclination angle of the substrate, allowing an *a priori* prediction of the shape and dispersion of solitary waves for a given fluid. The presented results and observed correlations provide a detailed account of the acting physical mechanisms that drive and influence the dynamic behavior of solitary waves.

In Sec. II the governing equations are discussed briefly and in Sec. III a new scaling for solitary waves is proposed. The applied numerical methodology is briefly outlined in Sec. IV, and Sec. V describes the setup and parameter space of the conducted numerical experiments. A detailed analysis of the shape of solitary waves is presented in Sec. VI, followed by an analysis of the nonlinear dispersion of solitary waves in Sec. VII. We close with a summary of our findings in Sec. VIII.

II. GOVERNING EQUATIONS

The dynamic behavior of isothermal, Newtonian fluids in the incompressible flow regime is governed by the momentum equations

$$\rho\left(\frac{\partial u_i}{\partial t} + u_j\frac{\partial u_i}{\partial x_j}\right) = -\frac{\partial p}{\partial x_i} + \frac{\partial}{\partial x_j}\left[\mu\left(\frac{\partial u_i}{\partial x_j} + \frac{\partial u_j}{\partial x_i}\right)\right] + \rho\, g_i + f_{\sigma,i} \tag{1}$$

and the continuity equation

$$\frac{\partial u_i}{\partial x_i} = 0, \tag{2}$$

where $\boldsymbol{x} \equiv (x,y,z)$ denotes a Cartesian coordinate system with x in the streamwise direction, y is cross-stream direction, and z the transverse direction (we adopt the Einstein notation), t represents time, $\boldsymbol{u}$ is the velocity, p is the pressure, ρ is the density, μ is the dynamic viscosity, $\boldsymbol{g}$ is the gravitational acceleration, and $\boldsymbol{f}_\sigma$ is the volumetric force due to surface tension acting at the gas-liquid interface. In falling liquid films in particular, the hydrodynamic balance of forces acting at the gas-liquid interface is given as [50]

$$(p_\mathrm{g} - p_\mathrm{l} + \sigma\,\kappa)\hat{m}_i = \left[\mu_\mathrm{g}\left(\left.\frac{\partial u_i}{\partial x_j}\right|_\mathrm{g} + \left.\frac{\partial u_j}{\partial x_i}\right|_\mathrm{g}\right) - \mu_\mathrm{l}\left(\left.\frac{\partial u_i}{\partial x_j}\right|_\mathrm{l} + \left.\frac{\partial u_j}{\partial x_i}\right|_\mathrm{l}\right)\right]\hat{m}_j - \frac{\partial\sigma}{\partial x_i}, \tag{3}$$

where subscript g denotes the gas phase, subscript l denotes the liquid phase, σ is the surface tension coefficient, κ is the curvature of the gas-liquid interface, and $\hat{\boldsymbol{m}}$ is the outward (pointing into the liquid phase) unit normal vector of the gas-liquid interface.

III. PARAMETRIZATION AND SCALING OF SOLITARY WAVES

Consider a laminar, falling liquid film flowing down a planar inclined substrate with angle β to the horizontal, schematically illustrated in Fig. 1. If this film is undisturbed, i.e., the film is flat and no external perturbations act on the film, a

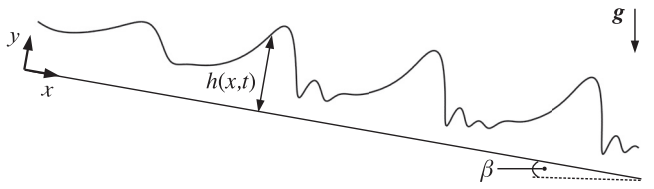

FIG. 1. Sketch of a liquid film on a substrate with inclination angle β to the horizontal. $h(x,t)$ is the local film thickness with respect to a Cartesian coordinate system (x,y) with x the streamwise coordinate and y the outward-pointing coordinate normal to the substrate. The origin of the coordinate system is on the substrate at the domain inlet.

unique equilibrium solution exists, called the *Nusselt flat film solution* [21,51]. The associated equilibrium flat film height (Nusselt film height) is

$$h_{\mathrm{N}} = \sqrt[3]{\frac{3\mu_{\mathrm{l}} q}{\rho_{\mathrm{l}} g \sin\beta}} \tag{4}$$

and the corresponding average film velocity (Nusselt velocity) is

$$u_{\mathrm{N}} = \frac{g \sin\beta \rho_{\mathrm{l}} h_{\mathrm{N}}^2}{3\mu_{\mathrm{l}}}, \tag{5}$$

where q is the flow rate per unit span, g is the magnitude of the gravitational acceleration, and subscript l denotes properties of the liquid film. The Nusselt flat film solution typically serves as the basis for the characterization of laminar, gravity-driven film flows and the associated interfacial instabilities.

A. Physical mechanisms and pertinent dimensionless groups

Three physical mechanisms dominate the dynamic behavior of free-surface flows: inertia, viscous stresses, and surface tension. Each of these effects can be quantified by their respective pressure scales, namely, the dynamic pressure

$$p_{\mathrm{dyn}} = \frac{\rho_{\mathrm{l}} u_{\mathrm{N}}^2}{2}, \tag{6}$$

the viscous pressure

$$p_{\mu} = \frac{\mu_{\mathrm{l}} u_{\mathrm{N}}}{h_{\mathrm{N}}}, \tag{7}$$

and the pressure due to surface tension

$$p_{\sigma} = \frac{\sigma}{h_{\mathrm{N}}}. \tag{8}$$

The relative importance of these three mechanisms can be unraveled by making use of the Reynolds number

$$\mathrm{Re} = \frac{2p_{\mathrm{dyn}}}{p_{\mu}} = \frac{\rho_{\mathrm{l}} u_{\mathrm{N}} h_{\mathrm{N}}}{\mu_{\mathrm{l}}} = \frac{\rho_{\mathrm{l}} q}{\mu_{\mathrm{l}}}, \tag{9}$$

which compares inertia and viscous effects, the Weber number

$$\mathrm{We} = \frac{2p_{\mathrm{dyn}}}{p_{\sigma}} = \frac{\rho_{\mathrm{l}} h_{\mathrm{N}} u_{\mathrm{N}}^2}{\sigma}, \tag{10}$$

which compares the inertia of the film flow to the surface tension of the interface, and the capillary number

$$\mathrm{Ca} = \frac{p_{\mu}}{p_{\sigma}} = \frac{\mu_{\mathrm{l}} u_{\mathrm{N}}}{\sigma} = \frac{\rho_{\mathrm{l}} g \sin\beta h_{\mathrm{N}}}{3\sigma}, \tag{11}$$

which compares viscous effects and surface tension. All three nondimensional numbers are related to each other as $\mathrm{We} = \mathrm{Re}\,\mathrm{Ca}$. In the context of falling liquid films the Reynolds number Re can also be regarded as the nondimensional flow rate. Using the scalings introduced by Shkadov [52] for falling liquid films, the Weber number can be written as $\mathrm{We} = \delta\eta/9$, where $\delta = 3\,\mathrm{Re}\,(3\,\mathrm{Ca})^{1/3}$ is the reduced Reynolds number and $\eta = (3\,\mathrm{Ca})^{2/3}$ is the viscous dispersion number [21].

In the literature on falling liquid films, notably [21,53,54], the inverse of the capillary number Ca is referred to at times as a Weber number $\mathrm{We}_{\mu} = 1/3\,\mathrm{Ca}$, where the subscript μ indicates its association with viscous stresses. This presumably stems from the fact that most theoretical studies to date have focused on film flows with low inertia in which the balance of viscous stresses and surface tension plays a dominant role, a regime which can be adequately described using models based on the boundary-layer approximation (e.g., [19,21,36,52,55–57]). The Weber number We given in Eq. (10), on the other hand, is widely used in the context of inertia-dominated two-phase flows, such as liquid jets, bubbles, and drops (e.g., [58–62]). It is important to note that some studies on film flows use a Weber number defined as the inverse of We as defined in Eq. (10), for instance [3,19,63–65].

Apart from the properties of the liquid and the inclination angle of the substrate, the Reynolds number, Weber number, and capillary number depend on h_{N}, which in experiments can be modified by changing the flow rate $q = h_{\mathrm{N}} u_{\mathrm{N}}$. The Kapitza number Ka, on the other hand, only depends on the selected fluid and the inclination angle of the substrate,

$$\mathrm{Ka} = \frac{\sigma}{\rho_{\mathrm{l}} \nu_{\mathrm{l}}^{4/3} (g \sin\beta)^{1/3}} = \frac{\mathrm{Re}^{2/3}}{3^{1/3}\,\mathrm{Ca}}, \tag{12}$$

with $\nu_{\mathrm{l}} = \mu_{\mathrm{l}}/\rho_{\mathrm{l}}$ being the kinematic viscosity of the liquid film, providing a universal measure of the relative importance of surface tension and inertia in a falling liquid film. Hence, for fixed liquid properties and a fixed inclination angle β, the Kapitza number is constant and the only free parameter is the Reynolds number (through the flow rate).

B. Inclination-corrected scaling

An interfacial wave evolving from a long-wave perturbation is always unstable (for all Re) on a vertically falling liquid film ($\beta = 90^{\circ}$) and stable on a horizontal liquid film ($\beta = 0^{\circ}$) [21]. Consequently, since the horizontal component of velocity does not contribute to sustaining the solitary wave, a fully developed solitary wave is only affected by the vertical component of the velocity, leading to the reference velocity

$$u_{\mathrm{N}}^{*} = u_{\mathrm{N}} \sin\beta = \frac{g(\sin\beta)^2 \rho_{\mathrm{l}} h_{\mathrm{N}}^2}{3\mu_{\mathrm{l}}}, \tag{13}$$

henceforth referred to as *driving Nusselt velocity*.

Based on the driving Nusselt velocity u_{N}^{*}, the effective dynamic pressure of the liquid film becomes

$$p_{\mathrm{dyn}}^{*} = \frac{\rho_{\mathrm{l}} u_{\mathrm{N}}^{*2}}{2} = \frac{\rho_{\mathrm{l}} u_{\mathrm{N}}^{2}}{2} (\sin\beta)^2, \tag{14}$$

and, similarly, the effective viscous pressure follows as

$$p_{\mu}^{*} = \frac{\mu_{\mathrm{l}} u_{\mathrm{N}}^{*}}{h_{\mathrm{N}}} = \frac{\mu_{\mathrm{l}}\, u_{\mathrm{N}}}{h_{\mathrm{N}}} \sin\beta. \tag{15}$$

The pressure due to surface tension p_{σ} remains unchanged, as defined in Eq. (8), since the influence of surface tension does not depend on the velocity of the flow or the orientation of the gas-liquid interface. Consequently, the driving Reynolds number, the driving Weber number, and the driving capillary number (i.e., the nondimensional numbers based on the driving Nusselt velocity) follow as

$$\mathrm{Re}^{*} = \frac{2p_{\mathrm{dyn}}^{*}}{p_{\mu}^{*}} = \frac{\rho_{\mathrm{l}} u_{\mathrm{N}}^{*} h_{\mathrm{N}}}{\mu_{\mathrm{l}}} = \mathrm{Re}\,\sin\beta, \tag{16}$$

$$\mathrm{We}^{*} = \frac{2p_{\mathrm{dyn}}^{*}}{p_{\sigma}} = \frac{\rho_{\mathrm{l}} h_{\mathrm{N}} u_{\mathrm{N}}^{*2}}{\sigma} = \mathrm{We}(\sin\beta)^2, \tag{17}$$

$$\mathrm{Ca}^{*} = \frac{p_{\mu}^{*}}{p_{\sigma}} = \frac{\mu_{\mathrm{l}} u_{\mathrm{N}}^{*}}{\sigma} = \mathrm{Ca}\,\sin\beta. \tag{18}$$

All three driving nondimensional numbers are related to each other as $\mathrm{We}^{*} = \mathrm{Re}^{*}\mathrm{Ca}^{*}$.

IV. NUMERICAL METHODOLOGY

DNS of the full two-phase system, including the liquid film, the gas phase, as well as the gas-liquid interface, are conducted by resolving all relevant length and time scales. The governing equations are solved numerically using a state-of-the-art finite-volume framework for interfacial flows, described in detail in Ref. [47]. The primitive variables are solved in a single linear system of equations using a coupled, implicit finite-volume framework with collocated variable arrangement. The momentum equations, Eq. (1), are discretized using a second-order backward Euler scheme for the transient term, while the convection, diffusion, and pressure terms are discretized using a central differencing scheme. The continuity equation, Eq. (2), is discretized using a balanced-force implementation of the momentum-weighted interpolation method, proposed by Denner and van Wachem [47], which couples pressure and velocity. Each time step consists of a finite number of nonlinear iterations to account for the nonlinearity of the governing equations, updating the deferred terms of the equation system based on the result of the previous nonlinear iteration [66]. This iterative procedure continues until the nonlinear problem has converged to a sufficiently small tolerance.

The volume-of-fluid (VOF) method [67] is adopted to capture the interface between the immiscible gas and liquid bulk phases. The local volume fraction of both phases in each mesh cell is represented by the color function γ, defined as $\gamma = 0$ in the gas phase and $\gamma = 1$ in liquid phase, with the interface located in mesh cells with a color function value of $0 < \gamma < 1$. The local density ρ and viscosity μ are defined based on the color function γ as

$$\rho(\boldsymbol{x}) = \rho_{\mathrm{g}}[1 - \gamma(\boldsymbol{x})] + \rho_{\mathrm{l}}\gamma(\boldsymbol{x}), \tag{19}$$

$$\mu(\boldsymbol{x}) = \mu_{\mathrm{g}}[1 - \gamma(\boldsymbol{x})] + \mu_{\mathrm{l}}\gamma(\boldsymbol{x}), \tag{20}$$

respectively. The color function γ is advected by the linear hyperbolic equation

$$\frac{\partial \gamma}{\partial t} + u_i \frac{\partial \gamma}{\partial x_i} = 0 \tag{21}$$

based on the underlying flow with velocity $\boldsymbol{u}$. Equation (21) is discretized using a compressive VOF methodology [48], based on the compressive interface capturing scheme for arbitrary meshes scheme [68].

Assuming a constant surface tension coefficient σ and neglecting mass transfer between the bulk phases, the surface force per unit volume is described by the continuum surface force model [69] as

$$f_{\sigma,i} = \sigma\kappa \frac{\partial \gamma}{\partial x_i}, \tag{22}$$

which translates the surface force resulting from surface tension into a volume force which can be discretized in a finite volume framework. To ensure a balanced-force implementation of the surface force, Eq. (22) is discretized on the same computational stencil as the pressure gradient [47]. In order to diminish aliasing errors in the evaluation of the interface normal vector $\hat{\boldsymbol{m}} = \nabla\gamma/|\nabla\gamma|$ and the interface curvature $\kappa = -\nabla\cdot\hat{\boldsymbol{m}}$, the volume fraction γ is convoluted by means of a cosine convolution kernel with a support of $\varepsilon = 3\Delta x$, where Δx is the mesh spacing [37,47,70]. Convolution to smooth the surface force is not needed [71,72] and numerical artifacts that manifest in parasitic or spurious flow features near or at the interface are addressed by an interfacial shear stress correction [37].

Simulation results obtained with this numerical framework have been shown to be in excellent agreement with analytical solutions and experimental data for single-phase flows [73,74], interfacial flows in general [47,48,71–73], and solitary waves on falling liquid films [37] in particular.

V. SETUP OF THE NUMERICAL EXPERIMENTS

The shape and dispersion of solitary waves with constant frequency $f = 20\ \mathrm{s}^{-1}$ on 34 different falling water films in contact with air are simulated and analyzed for different Reynolds numbers Re, on substrates with different inclination angles β and for different surface tension coefficients σ. The working fluid is taken to be water with a density of $\rho_{\mathrm{l}} = 998\ \mathrm{kg\,m^{-3}}$ and a viscosity of $\mu_{\mathrm{l}} = 8.967 \times 10^{-4}$ Pa s, air is taken to have a density of $\rho_{\mathrm{g}} = 1.17\ \mathrm{kg\,m^{-3}}$ and a viscosity of $\mu_{\mathrm{g}} = 1.836 \times 10^{-5}$ Pa s. All relevant parameters of the different cases analyzed are given in Table I.

These cases can be divided into three groups of results. The first group consists of 23 cases with $\mathrm{Re} = 20$–120 and a surface tension coefficient of $\sigma = 0.072\ \mathrm{N\,m^{-1}}$, with inclination angles $\beta = 45^{\circ}$, $\beta = 60^{\circ}$, $\beta = 75^{\circ}$, and $\beta = 90^{\circ}$. The second group of results includes 15 cases with $\mathrm{Re} = 20$–100 on a substrate with inclination angle $\beta = 90^{\circ}$ and

TABLE I. Nondimensional numbers, inclination angle of the substrate β, and surface tension coefficient σ of the analyzed falling liquid films.

No.	Re	β	σ (N m^{-1})	We	Ca	Ka
1	20	60°	7.20×10^{-2}	2.51×10^{-2}	1.25×10^{-3}	4078
2	20	75°	7.20×10^{-2}	2.60×10^{-2}	1.30×10^{-3}	3932
3	20	90°	5.12×10^{-2}	3.70×10^{-2}	1.85×10^{-3}	2765
4	20	90°	6.21×10^{-2}	3.05×10^{-2}	1.53×10^{-3}	3349
5	20	90°	7.20×10^{-2}	2.63×10^{-2}	1.31×10^{-3}	3887
6	40	45°	7.20×10^{-2}	7.43×10^{-2}	1.86×10^{-3}	4363
7	40	60°	7.20×10^{-2}	7.95×10^{-2}	1.99×10^{-3}	4078
8	40	75°	7.20×10^{-2}	8.25×10^{-2}	2.06×10^{-3}	3932
9	40	90°	5.12×10^{-2}	1.17×10^{-1}	2.93×10^{-3}	2765
10	40	90°	6.21×10^{-2}	9.68×10^{-2}	2.42×10^{-3}	3349
11	40	90°	7.20×10^{-2}	8.35×10^{-2}	2.09×10^{-3}	3887
12	60	45°	7.20×10^{-2}	1.46×10^{-1}	2.44×10^{-3}	4363
13	60	60°	7.20×10^{-2}	1.56×10^{-1}	2.61×10^{-3}	4078
14	60	75°	7.20×10^{-2}	1.62×10^{-1}	2.70×10^{-3}	3932
15	60	90°	5.12×10^{-2}	2.31×10^{-1}	3.84×10^{-3}	2765
16	60	90°	6.21×10^{-2}	1.90×10^{-1}	3.17×10^{-3}	3349
17	60	90°	7.20×10^{-2}	1.64×10^{-1}	2.73×10^{-3}	3887
18	80	45°	7.20×10^{-2}	2.36×10^{-1}	2.95×10^{-3}	4363
19	80	60°	7.20×10^{-2}	2.53×10^{-1}	3.16×10^{-3}	4078
20	80	75°	7.20×10^{-2}	2.62×10^{-1}	3.27×10^{-3}	3932
21	80	90°	5.12×10^{-2}	3.72×10^{-1}	4.66×10^{-3}	2765
22	80	90°	6.21×10^{-2}	3.07×10^{-1}	3.84×10^{-3}	3349
23	80	90°	7.20×10^{-2}	2.65×10^{-1}	3.31×10^{-3}	3887
24	100	19°	7.20×10^{-2}	2.65×10^{-1}	2.65×10^{-3}	5641
25	100	30°	7.20×10^{-2}	3.05×10^{-1}	3.05×10^{-3}	4897
26	100	45°	7.20×10^{-2}	3.42×10^{-1}	3.42×10^{-3}	4363
27	100	60°	7.20×10^{-2}	3.66×10^{-1}	3.66×10^{-3}	4078
28	100	75°	7.20×10^{-2}	3.80×10^{-1}	3.80×10^{-3}	3932
29	100	90°	6.21×10^{-2}	4.46×10^{-1}	4.46×10^{-3}	3349
30	100	90°	7.20×10^{-2}	3.84×10^{-1}	3.84×10^{-3}	3887
31	120	45°	7.20×10^{-2}	4.64×10^{-1}	3.87×10^{-3}	4363
32	120	60°	7.20×10^{-2}	4.96×10^{-1}	4.14×10^{-3}	4078
33	120	75°	7.20×10^{-2}	5.15×10^{-1}	4.29×10^{-3}	3932
34	120	90°	7.20×10^{-2}	5.21×10^{-1}	4.34×10^{-3}	3887

$\sigma = 0.0512$–0.0621 N m^{-1}. The third group of results are six cases with Re = 100 and a surface tension coefficient $\sigma = 0.072$ N m^{-1}, simulated on a substrate with inclination angles of $\beta = 19°$–$90°$. The chosen cases allow a detailed and comprehensive scrutiny of the influence of inertia, the inclination angle of the substrate, as well as surface tension on the equilibrium shape and dispersion of solitary waves.

The applied three-dimensional computational domain, schematically illustrated in Fig. 2, has the dimensions $300h_N \times 6h_N \times 0.1h_N$ (with $0.1h_N$ being the transverse dimension) and is represented by a Cartesian mesh. We found that a domain height of $L_y = 6h_N$ has a negligible effect on the dynamic behavior of the solitary waves. This is further supported by the study of Albert *et al.* [75] who concluded that a domain height of $L_y = 4h_N$ is sufficient. The region of the computational mesh in which the dynamically evolving gas-liquid interface is located has an equidistant resolution of ten cells per h_N, following the work of Albert *et al.* [75]. The mesh resolution gradually increases near the substrate, with the cell center of the mesh cells closest to the substrate located at a distance of $0.0035h_N$ from the substrate, assuring a detailed spatial resolution of the flow separation and reversal [4,38,39] in the wave troughs observed in some of the studied cases. We note that the transverse dimension is resolved with only one mesh cell, so that the simulation can be regarded as being effectively two dimensional. The numerical time step applied in the simulations satisfies a Courant number of $\mathrm{Co} = \Delta t_u |\boldsymbol{u}|/\Delta x \leqslant 0.25$, as well as the capillary time-step constraint proposed by Denner and van Wachem [49].

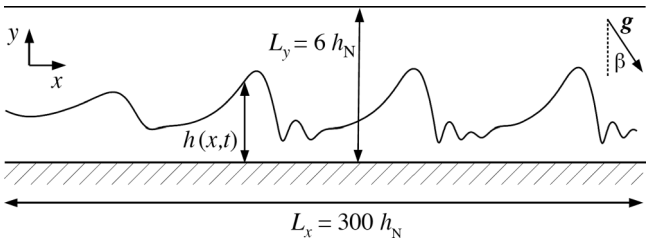

FIG. 2. Sketch of the numerical domain with the liquid film of height $h(x,t)$ on a substrate with inclination angle β.

At the substrate a no-slip condition is enforced and at the top (gas-side) boundary a free-slip and no-penetration boundary condition is applied. A monochromatic forcing is imposed at the domain inlet by periodically changing the flow rate with frequency $f = 20$ s^{-1} and amplitude A from the mean. The amplitude is chosen in order to obtain fully developed waves within the finite length of the computational domain. At the domain inlet a semiparabolic velocity profile is prescribed for the liquid phase,

$$u(x = 0, 0 \leqslant y \leqslant h_N) = \frac{3}{2}[1 + A\ \sin(2\pi f t)] \times \left(\frac{2y}{h_N} - \frac{y^2}{h_N^2}\right) u_N, \quad (23)$$

and a spatially invariant velocity is prescribed for the gas phase,

$$u(x = 0, h_N < y \leqslant 6h_N) = \tfrac{3}{2}[1 + A\ \sin(2\pi f t)]u_N. \quad (24)$$

The film height at the inlet is constant, $h(x = 0) = h_N$. The domain outlet is modeled as an open boundary, following Nosoko and Miyara [46] and Denner *et al.* [37], with

$$\left.\frac{\partial u_i}{\partial x}\right|_{\text{out}} = \left.\frac{\partial p}{\partial x}\right|_{\text{out}} = 0, \quad (25)$$

which assures that the flow can leave the domain with minimal reflections. Initially, at time $t = 0$ s, the film is flat and the velocity field is fully developed.

VI. SHAPE OF SOLITARY WAVES

The instantaneous film height h/h_N as a function of the downstream distance x/h_N for a representative selection of the considered cases is shown in Figs. 3 and 4. The maximum film height (i.e., height of the crest of the solitary wave) exhibits a clear dependency on the inclination angle β and the surface tension coefficient σ, whereas the minimum film height (i.e., height of the trough preceding the solitary wave) is independent of β and σ for high Reynolds numbers. Similarly,

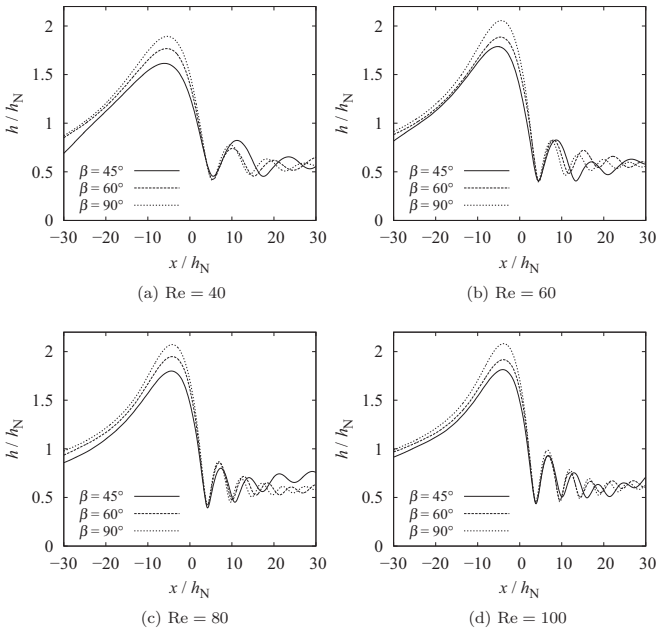

(a) Re = 40 (b) Re = 60 (c) Re = 80 (d) Re = 100

FIG. 3. Interface height h of the falling water film as a function of downstream distance x, both normalized by the Nusselt film height h_N, with $x = 0$ located at the center of the front of the solitary wave, for selected cases of different Reynolds numbers Re and inclination angles β.

the influence of the inclination angle and the surface tension coefficient on the number and amplitude of capillary ripples preceding the main solitary hump reduces for increasing Reynolds number, which is particularly relevant for the onset of flow separation [4,37–39] as well as the wave length and binary interactions of solitary waves [12,13].

A. Maximum film height

Figure 5 shows the maximum and minimum film height, normalized by the Nusselt film height h_N, as a function of the driving nondimensional numbers defined in Sec. III B. As noted in the previous paragraph, the inclination angle has a strong influence on the maximum film height h_{max}, which is the result of gravity acting in the cross-stream direction, arresting the growth of the solitary wave at a smaller maximum film height for smaller inclination angles. Similarly, a higher surface tension coefficient means the growth of the solitary wave is arrested at a lower equilibrium film height, as surface tension acts to flatten the wave. The initial increase of the maximum film height for $\mathrm{Re}^* \lesssim 60$ correlates very well (i.e., the data collapse into a single curve) with the driving Reynolds number Re^* and the driving Weber number We^*. The correlation with We^* also holds if the surface tension coefficient changes, as seen in Fig. 6. For changing inclination angle β but constant Reynolds number Re, the maximum film height is monotonically increasing, shown in Fig. 7. This suggests that, apart from the influence of the cross-stream component of gravity, the maximum film height is also affected by the balance of surface tension and the driving component of inertia.

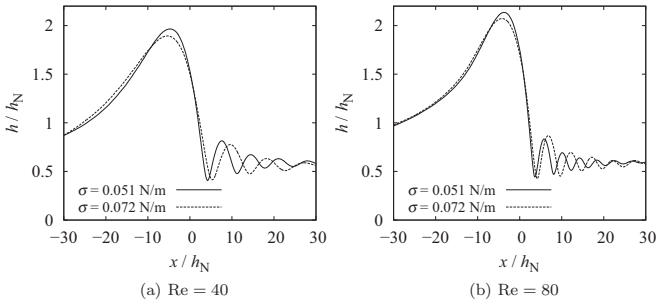

(a) Re = 40 (b) Re = 80

FIG. 4. Interface height h of the falling water film as a function of downstream distance x, both normalized by the Nusselt film height h_N, with $x = 0$ located at the center of the front of the solitary wave, for selected cases of different Reynolds numbers Re and surface tension coefficients σ.

B. Minimum film height

As observed in Fig. 3, the cases with $\mathrm{Re}^* \gtrsim 60$ have a common minimum film height which is independent of the inclination angle. Plotting the minimum film height for all cases as a function of the three proposed driving nondimensional numbers in Figs. 5–7, reveals a global minimum of the minimum film height of $h_{min} = 0.37 h_N \pm 1.1\%$ for all considered cases, as indicated by the dotted lines in the figures. When the surface tension coefficient remains unaltered, the minimum film height is correlated with all three driving nondimensional numbers (see Fig. 5), whereas comparing the cases with different surface tension coefficients the minimum film height is predominantly a function of the driving Weber number We^* (see Fig. 6). For Re = 100 and inclination angle $\beta = 19°$–$90°$, shown in Fig. 7, the minimum film height remains approximately constant irrespective of the inclination angle.

The deepening of the trough preceding the solitary wave competes with the decelerating forces imposed by viscous stresses near the substrate (the crest and trough of a fully developed solitary wave travel with the same speed [12,76]), surface tension which acts to flatten the film, as well as the narrowing cross-section of the film as a result of the wave trough approaching the substrate. The minimum film height, hence, represents the balance of inertia with viscous stresses and surface tension at the trough preceding the solitary wave, as shown by the correlation of the minimum film height with the driving Reynolds number Re^* and the driving Weber number We^* for all considered inclination angles and surface tension coefficients.

The observed initial decrease of the minimum film height for increasing Reynolds number when $\mathrm{Re}^* \lesssim 60$, with a minimum at $\mathrm{Re}^* \approx 60$, followed by an increase of the minimum film height when $\mathrm{Re}^* \gtrsim 60$ corresponds well with the findings of Chakraborty *et al.* [44] concerning the onset of flow separation underneath the trough preceding the solitary wave. Chakraborty *et al.* [44] reported that for sufficiently high flow rates, inertia overcomes the adverse pressure gradient imposed by the convex shape of the interface at the trough preceding the solitary wave, since the low pressure region underneath the wave trough cannot extend into the low velocity region near the substrate, as shown by Denner *et al.* [37].

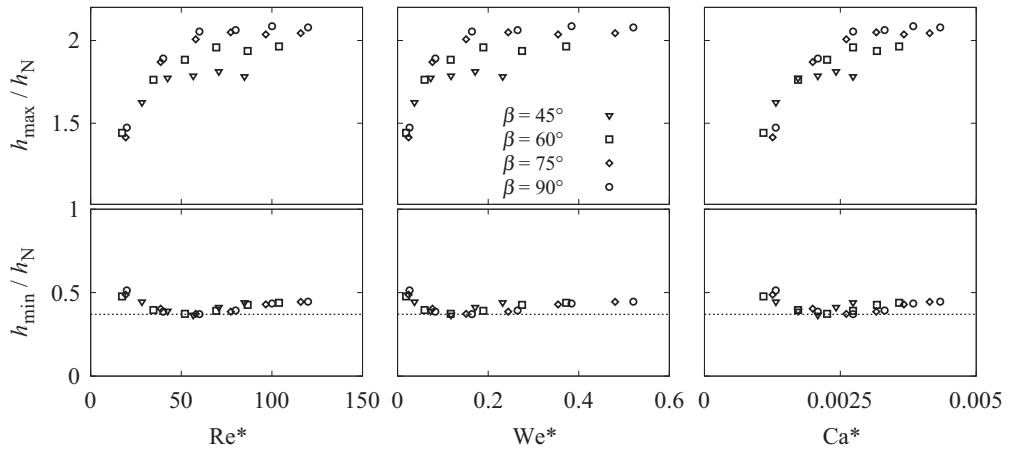

FIG. 5. Maximum film height h_{max} and minimum film height h_{min}, normalized by the Nusselt height h_N, as a function of driving Reynolds number Re*, driving Weber number We*, and driving capillary number Ca* for different inclination angles β. The dotted line represents the global minimum film height of $0.37h_N$.

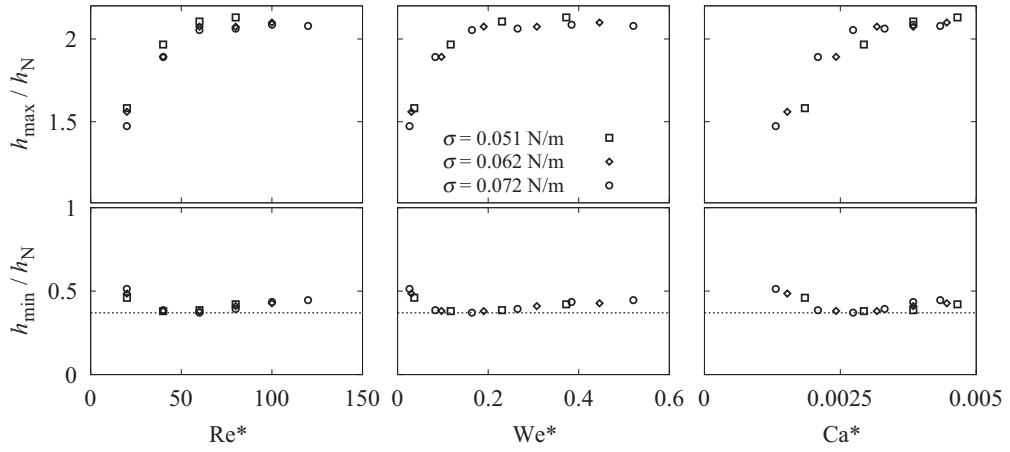

FIG. 6. Maximum film height h_{max} and minimum film height h_{min}, normalized by the Nusselt height h_N, as a function of driving Reynolds number Re*, driving Weber number We*, and driving capillary number Ca*, at an inclination angle $\beta = 90°$, for different surface tension coefficients σ. The dotted line represents the global minimum film height of $0.37h_N$.

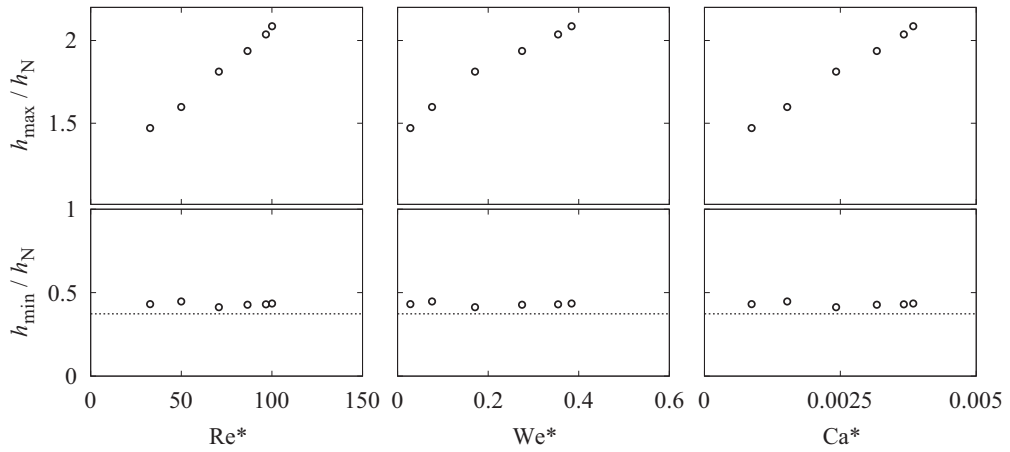

FIG. 7. Maximum film height h_{max} and minimum film height h_{min}, normalized by the Nusselt height h_N, as a function of driving Reynolds number Re*, driving Weber number We*, and driving capillary number Ca* for Re $= 100$ and inclination angles $\beta = 19°$–$90°$. The dotted line represents the global minimum film height of $0.37h_N$.

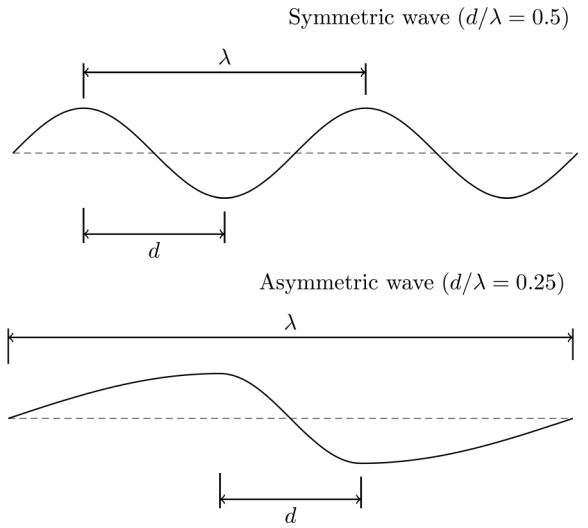

FIG. 8. Sketch of an example of the symmetry and asymmetry of a the main wave hump, with the length d of the wave front and the wavelength λ.

C. Asymmetry of the solitary wave

We look now at the length d of the front of the solitary wave, which is defined as the distance between the crest of the solitary wave and the trough immediately downstream from the main wave hump, normalized by the wavelength λ of the solitary wave. With respect to solitary waves, the wavelength λ defines the length of the entire pulse, including the main wave hump and the preceding capillary ripples. The ratio d/λ can be regarded as a measure of the asymmetry of the solitary wave, with $d/\lambda = 0.5$ representing a fully "symmetric wave" (as far as solitary waves on falling liquid films are concerned, symmetric waves are only observed at low Reynolds numbers and close to the domain inlet), as illustrated in Fig. 8.

An increasing inertia of the liquid film leads to a steepening of the wave front (i.e., smaller d/λ) and, thus, increasing asymmetry of the solitary wave. Figures 9–11 depict the length d of the solitary wave, where we can see that this asymmetry is correlated with the driving Weber number We^* and is, consequently, governed by the balance of inertia and surface tension,

$$\frac{d}{\lambda} \sim \frac{1}{\sqrt{\mathrm{We}^*}} = \sqrt{\frac{p_\sigma}{2p^*_{\mathrm{dyn}}}}. \tag{26}$$

This correlation holds irrespective of the inclination angle (see Figs. 9 and 11) or the surface tension coefficient (see Fig. 10). The driving dynamic pressure p^*_{dyn} of the flow acts to steepen the wave and, thus, reduces the length d of the wave front, whereas surface tension acts to increase the length of the wave front, leading to a shallower front of the solitary wave. Furthermore, the asymmetry of the solitary wave is not correlated with the driving capillary number Ca^*, suggesting that the balance of surface tension and viscous stresses, which is a main assumption for low-dimensional models valid typically in the region of low Re (see, e.g., [19,21,36,55–57]) is not really appropriate for inertia-dominated film flows. Hence, surface tension balances the inertia of the liquid film at the wave front, and it is this balance that governs the asymmetry of the solitary wave. If the vertical component of inertia and the inclination angle of the substrate are sufficiently high, the surface tension of the gas-liquid interface is no longer able to balance the inertia of the liquid film and the solitary wave breaks as a result [19,77,78].

VII. DISPERSION OF SOLITARY WAVES

To gain a better understanding of the dispersion of solitary waves, linear wave theory (describing the frequency dispersion of capillary-gravity waves and capillary waves of small amplitude) lends itself for a comparison with the dispersion of solitary waves. A capillary-gravity wave with wave number k propagates on a film of height h_{N} with phase velocity [79,80]

$$c_{\sigma\text{-g}} = \sqrt{\left(\frac{\sigma k}{\rho_{\mathrm{l}}} + \frac{g\,\cos\beta}{k}\right)\tanh(kh_{\mathrm{N}})}, \tag{27}$$

whereas a pure capillary wave propagates with phase velocity

$$c_\sigma = \sqrt{\frac{\sigma k}{\rho_{\mathrm{l}}}\tanh(kh_{\mathrm{N}})}, \tag{28}$$

assuming $\rho_l \gg \rho_g$ and the fluids being inviscid. Given the relatively long wavelength of the considered cases, viscous

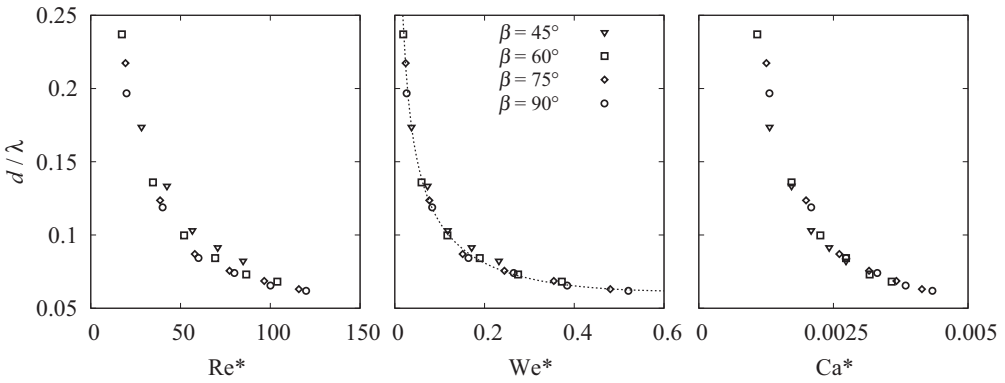

FIG. 9. Length d of the front of the solitary wave normalized by the wavelength λ as a function of driving Reynolds number Re^*, driving Weber number We^*, and driving capillary number Ca^* for different inclination angles β. The dotted line represents the function $d/\lambda = \mathcal{A}\,(\mathrm{We}^*)^{-1/2} + \mathcal{B}\,\mathrm{We}^*$, with coefficients $\mathcal{A}$ and $\mathcal{B}$ fitted to the data of the cases with $\beta = 90°$ and $\sigma = 0.072\ \mathrm{N\,m^{-1}}$.

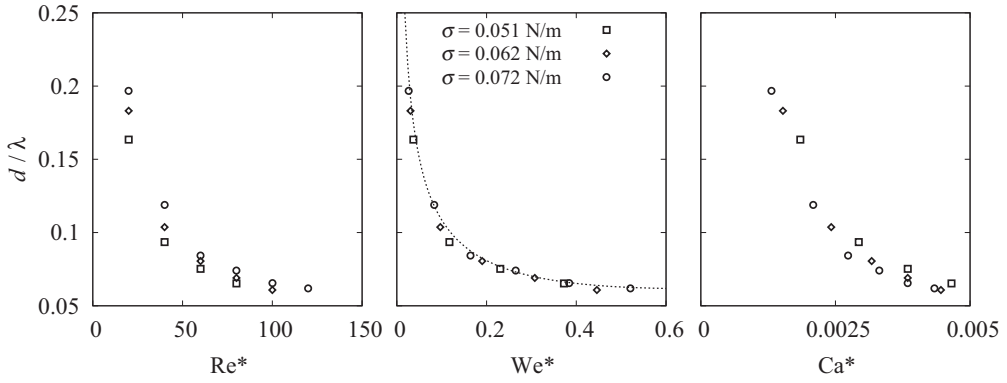

FIG. 10. Length d of the front of the solitary wave normalized by the wavelength λ as a function of driving Reynolds number Re^*, driving Weber number We^*, and driving capillary number Ca^*, at an inclination angle $\beta = 90^\circ$, for different surface tension coefficients σ. The dotted line represents the function $d/\lambda = \mathcal{A}\,(\mathrm{We}^*)^{-1/2} + \mathcal{B}\,\mathrm{We}^*$, with coefficients $\mathcal{A}$ and $\mathcal{B}$ fitted to the data of the cases with $\beta = 90^\circ$ and $\sigma = 0.072\ \mathrm{N\,m^{-1}}$.

damping of the wave dispersion can be neglected [81,82] and the fluids can be assumed inviscid for the application of linear wave theory. However, linear wave theory and, thus, Eqs. (27) and (28) are only valid in the limit of small amplitudes when $(h_{\max} - h_\mathrm{N})/h_\mathrm{N} \ll 1$ [83].

Taking the ratio of the net phase velocity of the solitary wave, $c_0 = c - u_\mathrm{N}$ (i.e., the phase velocity at which the solitary wave propagates relative to the film flow), and the phase velocity of a capillary-gravity wave $c_{\sigma\text{-g}}$ with the same wave number $k = 2\pi/\lambda$ (see Fig. 12), no direct correlation with the driving nondimensional numbers can be identified, as the dispersion of the solitary waves depends strongly on the inclination angle β. However, the ratio of the net phase velocity of the solitary wave c_0 and of the phase velocity of a capillary wave c_σ with the same wave number k correlates well with all three driving nondimensional numbers, in particular the driving Weber number We^*, as demonstrated in Fig. 13. By changing the surface tension coefficient, it becomes clear that the net phase velocity ratio is correlated with the driving Weber number We^*, as shown in Fig. 14, hence

$$c_0 \sim c_\sigma \sqrt{\mathrm{We}^*}. \tag{29}$$

This correlation is also valid for a film with constant Reynolds number ($\mathrm{Re} = 100$) on substrates with different inclination angles β, shown in Fig. 15. Inserting the equations for the capillary phase velocity c_σ, Eq. (28), and the driving Weber number We^*, Eq. (17), the correlation given in Eq. (29) becomes

$$c_0 \sim \sqrt{\frac{\sigma k}{\rho_\mathrm{l}} \tanh(k h_\mathrm{N}) \frac{\rho_\mathrm{l} h_\mathrm{N} u_\mathrm{N}^{*2}}{\sigma}}, \tag{30}$$

$$c_0 \sim \sqrt{k h_\mathrm{N} \tanh(k h_\mathrm{N})}\, u_\mathrm{N}^*, \tag{31}$$

$$c_0 \sim D u_\mathrm{N}^*, \tag{32}$$

with $D = \sqrt{k h_\mathrm{N} \tanh(k\, h_\mathrm{N})}$. Hence, the dispersion of the solitary waves represented by the net phase velocity c_0 is independent of the surface tension coefficient.

The phase velocity c of the solitary waves, shown in Figs. 16–18, is monotonically increasing with increasing inertia, with

$$c \sim \sqrt{\mathrm{Re}^*} \tag{33}$$

for all considered cases. This confirms that the phase velocity is in fact independent of surface tension, suggested in the previous paragraph based on the correlation given in Eq. (32), in particular since Eq. (33) also holds if the surface tension

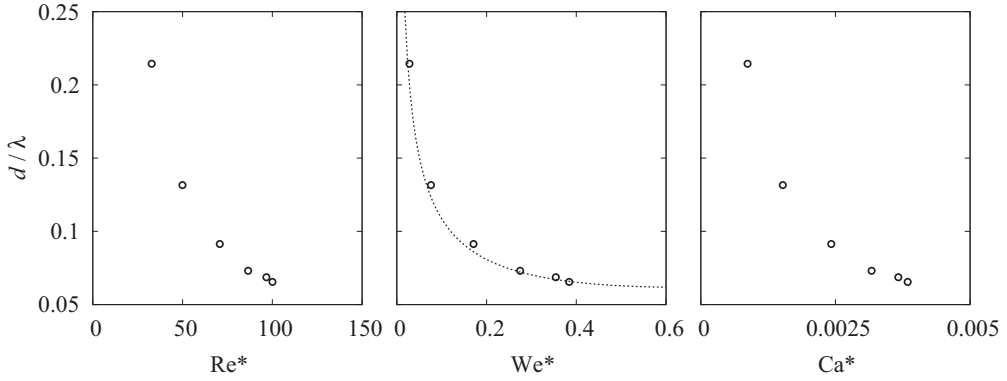

FIG. 11. Length d of the front of the solitary wave normalized by the wavelength λ as a function of driving Reynolds number Re^*, driving Weber number We^*, and driving capillary number Ca^* for $\mathrm{Re} = 100$ and inclination angles $\beta = 19^\circ$–90°. The dotted line represents the function $d/\lambda = \mathcal{A}\,(\mathrm{We}^*)^{-1/2} + \mathcal{B}\,\mathrm{We}^*$, with coefficients $\mathcal{A}$ and $\mathcal{B}$ fitted to the data of the cases with $\beta = 90^\circ$ and $\sigma = 0.072\ \mathrm{N\,m^{-1}}$.

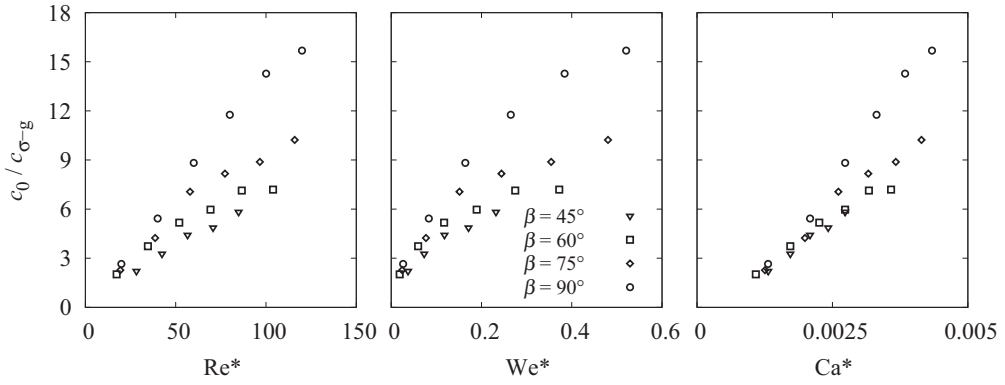

FIG. 12. Ratio of the net phase velocity of the solitary wave $c_0 = c - u_N$ and the phase velocity of a capillary-gravity wave $c_{\sigma\text{-}g}$ with the same wave number k as a function of driving Reynolds number Re^*, driving Weber number We^*, and driving capillary number Ca^* for different inclination angles β.

coefficient is changed (see Fig. 17). Since the train of solitary waves adopts the frequency f of the periodically changing mass flow at the inlet ($f = 20\ \mathrm{s}^{-1}$ in this study), the wavelength $\lambda = c/f$ exhibits the same relationship with respect to the driving Reynolds number, $\lambda \sim \sqrt{\mathrm{Re}^*}$, as the phase velocity c.

The presented results suggest that the dispersion of solitary waves is governed by inertia, with an increasing inertia of the film flow resulting in a higher phase velocity. Both correlations proposed in Eqs. (29) and (33) further suggest a strong influence of the substrate and the associated viscous stresses on the dispersion of solitary waves, since all parts of a

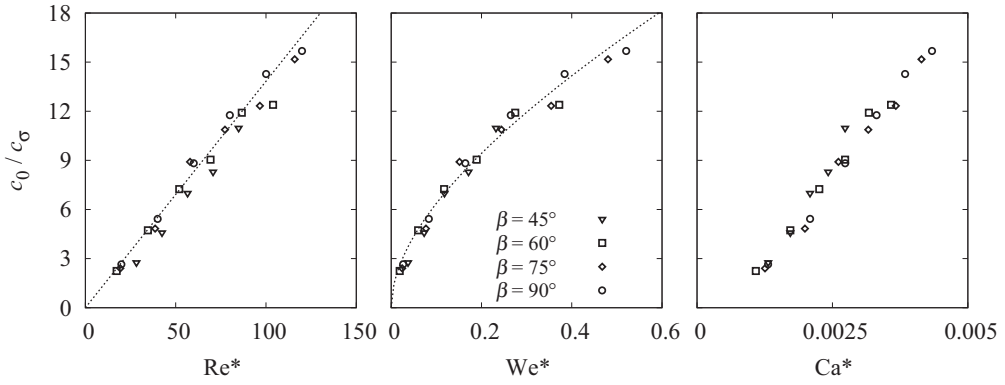

FIG. 13. Ratio of the net phase velocity of the solitary wave $c_0 = c - u_N$ and the phase velocity of a capillary wave c_σ with the same wave number k as a function of driving Reynolds number Re^*, driving Weber number We^*, and driving capillary number Ca^* for different inclination angles β. The dotted lines represent the functions $c_0/c_\sigma = \mathcal{A}\,\mathrm{Re}^*$ and $c_0/c_\sigma = \mathcal{B}\sqrt{\mathrm{We}^*} + \mathcal{C}\,\mathrm{We}^*$, respectively, with coefficients $\mathcal{A}$, $\mathcal{B}$, and $\mathcal{C}$ fitted to the data of the cases with $\beta = 90°$ and $\sigma = 0.072\ \mathrm{N\,m^{-1}}$.

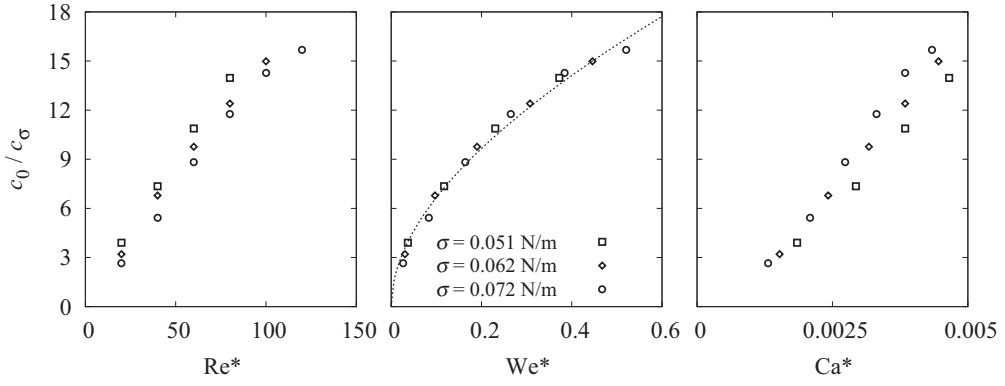

FIG. 14. Ratio of net phase velocity of the solitary wave $c_0 = c - u_N$ and the phase velocity of a capillary wave c_σ wave as a function of driving Reynolds number Re^*, driving Weber number We^*, and driving capillary number Ca^*, at an inclination angle $\beta = 90°$, for different surface tension coefficients σ. The dotted line represents the function $c_0/c_\sigma = \mathcal{A}\sqrt{\mathrm{We}^*} + \mathcal{B}\,\mathrm{We}^*$, with coefficients $\mathcal{A}$ and $\mathcal{B}$ fitted to the data of the cases with $\beta = 90°$ and $\sigma = 0.072\ \mathrm{N\,m^{-1}}$.

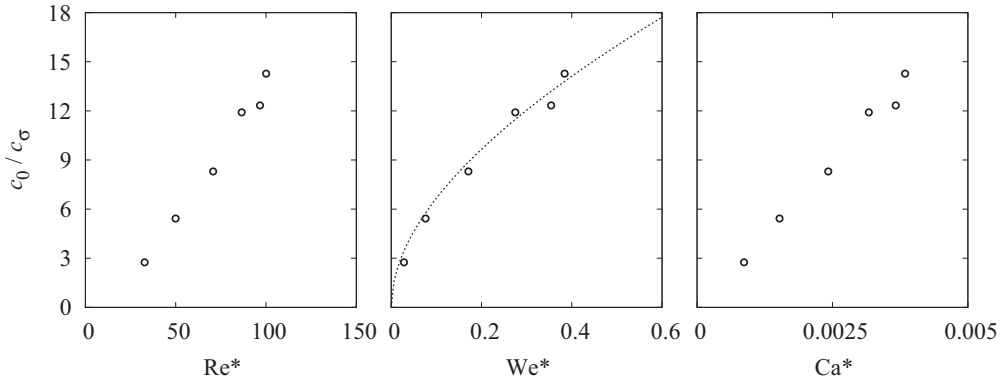

FIG. 15. Ratio of the net phase velocity of the solitary wave $c_0 = c - u_N$ and the phase velocity of a capillary wave c_σ with the same wave number k as a function of driving Reynolds number Re^*, driving Weber number We^*, and driving capillary number Ca^* for $\mathrm{Re} = 100$ and inclination angles $\beta = 19°$–$90°$. The dotted line represents the function $c_0/c_\sigma = \mathcal{A}\sqrt{\mathrm{We}^*} + \mathcal{B}\,\mathrm{We}^*$, with coefficients $\mathcal{A}$ and $\mathcal{B}$ fitted to the data of the cases with $\beta = 90°$ and $\sigma = 0.072\ \mathrm{N\,m^{-1}}$.

saturated solitary wave, including the wave trough preceding the main hump which is governed by viscous stresses near the substrate (see Sec. VI B), are propagating at the same speed. In particular, the absolute phase velocity of the analyzed solitary waves is a function of the ratio of inertia and viscous effects [see Eq. (33)]. Surface tension and gravity, on the other hand, have no discernible influence on the dispersion of solitary waves, contrary to the dispersion relation described by linear wave theory. Moreover, neither the net phase velocity ratio c_0/c_σ nor the phase velocity c are correlated with the driving capillary number Ca^* in a consistent manner, which further supports the observation that surface tension has a negligible influence on the dispersion of solitary waves. This behavior can be attributed to the considerable amplitude of solitary waves on inertia-dominated falling liquid films (see Sec. VI A) and the ensuing nonlinearity of the hydrodynamic system. The observed self-similarity of the dispersion of solitary waves, however, is dependent on the inclination angle of the substrate, resulting in the observed correlation with the driving Weber number We^*, Eq. (29), and the driving Reynolds number Re^*, Eq. (33). Since the phase velocity of a pure capillary wave, given in Eq. (28), is based on linear wave theory, the ratio c_0/c_σ can further be regarded as a measure of the nonlinearity of the dispersion of solitary waves, which is proportional to the proposed driving Nusselt velocity u_N^* of the falling liquid film.

VIII. CONCLUSIONS

We have scrutinized the solitary-wave characteristics, namely, maximum-minimum amplitude, phase velocity, and dispersion, as a function of the pertinent dimensionless parameters in inertia-dominated falling liquid films. We have proposed consistent scaling, derived from the Nusselt flat film solution based on the appropriate driving physical mechanisms, which leads to an unexpected self-similar characterization of solitary waves and allows an *a priori* description of the wave shape and dispersion.

Following a detailed analysis of the driving physical mechanisms and correlations with the proposed scaling of the main dimensionless numbers, our DNS results show a previously unknown self-similarity of the shape and dispersion of solitary waves. The correlations derived as part of the presented self-similar characterization of solitary waves follow directly from rational corrections to the relevant parameters and do not depend on any tunable coefficients.

Our results reveal that solitary waves on inertia-dominated falling liquid films are governed by a complex interplay of

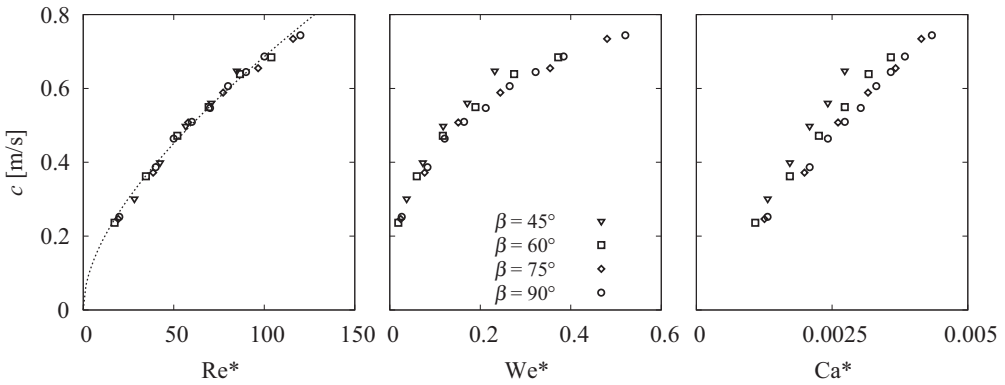

FIG. 16. Phase velocity c of the solitary wave as a function of driving Reynolds number Re^*, driving Weber number We^*, and driving capillary number Ca^* for different inclination angles β. The dotted line represents the function $c = \mathcal{A}\sqrt{\mathrm{Re}^*} + \mathcal{B}\,\mathrm{Re}^*$, with coefficients $\mathcal{A}$ and $\mathcal{B}$ fitted to the data of the cases with $\beta = 90°$ and $\sigma = 0.072\ \mathrm{N\,m^{-1}}$.

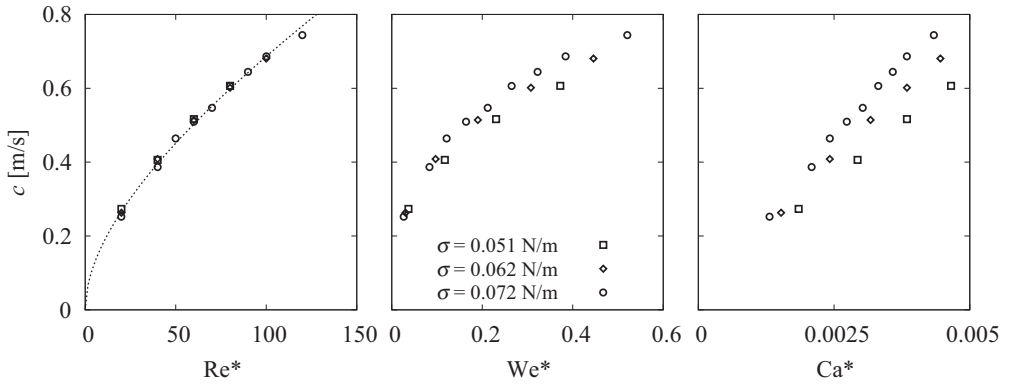

FIG. 17. Phase velocity c of the solitary wave as a function of driving Reynolds number Re^*, driving Weber number We^*, and driving capillary number Ca^*, for different surface tension coefficients σ. The dotted line represents the function $c = \mathcal{A}\sqrt{\mathrm{Re}^*} + \mathcal{B}\,\mathrm{Re}^*$, with coefficients $\mathcal{A}$ and $\mathcal{B}$ fitted to the data of the cases with $\beta = 90^\circ$ and $\sigma = 0.072\ \mathrm{N\,m^{-1}}$.

inertia, inclination angle of the substrate, viscous stresses in the vicinity of the substrate, as well as surface tension. Both the maximum and minimum film height exhibit strong correlations with the driving Reynolds number and the driving Weber number. The maximum film height (i.e., the height at the crest of the solitary wave) has been shown to depend on the inclination angle as well as surface tension, while viscosity has no discernible influence on the maximum film height. The minimum film height (i.e., the height of the trough preceding the main wave hump) has been shown to be governed by a balance of the inertia of the liquid film with viscous stresses in the vicinity of the substrate and the surface tension acting at the gas-liquid interface in the trough preceding the main wave hump. A global minimum of the minimum film height of $h_{\mathrm{min}} \approx 0.37 h_{\mathrm{N}}$ is observed. Furthermore, the asymmetry of solitary waves has been shown to depend on the balance of inertia and surface tension, with an increase in inertia resulting in a steeper wave front and, therefore, more asymmetric solitary wave.

The dispersion of solitary waves has been found to be governed by a balance of inertia and viscous stresses. The absolute phase velocity is correlated with the driving Reynolds number, whereas the net phase velocity ratio (ratio between net phase velocity of the solitary wave and a capillary wave with the same wave number but infinitesimal amplitude) is correlated with the driving Weber number. Further analysis showed that the net phase velocity of the solitary waves is proportional to the driving Nusselt velocity of the falling liquid film. These correlations persist irrespective of the inclination angle of the substrate or the surface tension coefficient of the gas-liquid interface, suggesting that the dispersion of the solitary waves in the inertia-dominated flow regime is dominated by inertia and that dispersion according to linear wave theory (i.e., frequency dispersion) has no significant influence.

The proposed scaling of the main dimensionless numbers allows one to predict the shape and phase velocity of a solitary wave on a falling liquid film of a given fluid with any flow rate (provided that the solitary wave does not break) and on a substrate with an arbitrary inclination angle, $0 \leqslant \beta \leqslant 90^\circ$, based on results at only two different flow rates or two different inclination angles.

Our computations also revealed that the (driving) capillary number is not suitable to describe, categorize, and predict the shape and dispersion of solitary waves on inertia-dominated falling liquid films. In our view this is a significant finding because many studies, including previously proposed low-dimensional models for interfacial instabilities on falling liquid

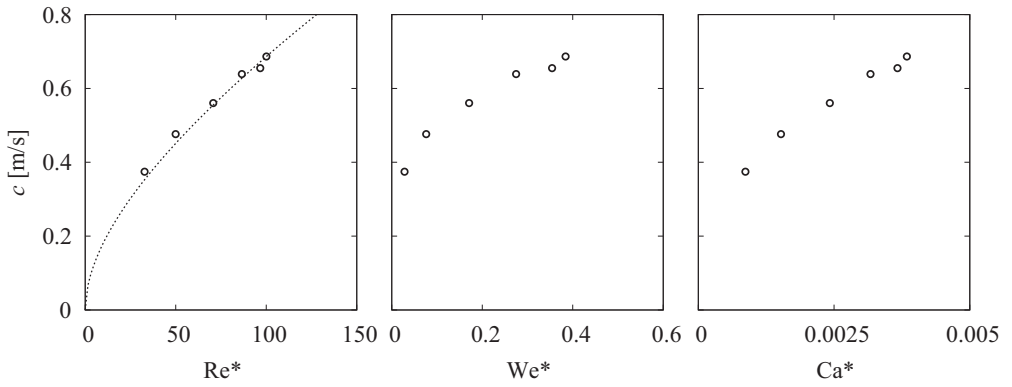

FIG. 18. Phase velocity c of the solitary wave as a function of driving Reynolds number Re^*, driving Weber number We^*, and driving capillary number Ca^* for $\mathrm{Re} = 100$ and inclination angles $\beta = 19^\circ$–90°. The dotted line represents the function $c = \mathcal{A}\sqrt{\mathrm{Re}^*} + \mathcal{B}\,\mathrm{Re}^*$, with coefficients $\mathcal{A}$ and $\mathcal{B}$ fitted to the data of the cases with $\beta = 90^\circ$ and $\sigma = 0.072\ \mathrm{N\,m^{-1}}$.

films, have used the capillary number or a similar formulation (e.g., inverse of the capillary number, usually referred to as the Weber number in these studies).

Even more important, our results indicate that despite their apparent complexity, film flows seem to be inherently simple nonlinear systems in that global quantities of interest can be described and understood in terms of simple relations. And self-similarity is at the heart of this "simplicity." It is also precisely the reason why in physics multiscale phenomena are amenable to a theoretical description in the first place. To put it simply, this means that phenomena can be appropriately reduced so that there are only a few dominant scales, and the "complexity" then is all in the transformation from one set of original scales to another. And in that respect, the falling film is rather similar to many other seemingly unrelated physical problems where self-similarity is prevalent.

ACKNOWLEDGMENTS

The authors acknowledge the financial support from the Engineering and Physical Sciences Research Council (EPSRC) of the UK through Grants No. EP/M021556/1 and No. EP/K008595/1. Data supporting this publication can be obtained from [84] under a Creative Common Attribution license.

[1] P. Kapitza, Z. Eksp. Teor. Fiz. **18**, 3 (1948).
[2] P. Kapitza and S. Kapitza, Z. Eksp. Teor. Fiz. **19**, 105 (1949).
[3] C. Meza and V. Balakotaiah, Chem. Eng. Sci. **63**, 4704 (2008).
[4] G. Dietze, A. Leefken, and R. Kneer, J. Fluid Mech. **595**, 435 (2008).
[5] G. Dietze, F. Al-Sibai, and R. Kneer, J. Fluid Mech. **637**, 73 (2009).
[6] A. Charogiannis, J. S. An, and C. N. Markides, Exp. Therm. Fluid Sci. **68**, 516 (2015).
[7] I. Zadrazil, O. Matar, and C. N. Markides, Int. J. Multiphase Flow **60**, 87 (2014).
[8] I. Zadrazil and C. N. Markides, Int. J. Multiphase Flow **67**, 42 (2014).
[9] E. A. Demekhin, E. N. Kalaidin, S. Kalliadasis, and S. Yu. Vlaskin, Phys. Fluids **19**, 114103 (2007).
[10] E. A. Demekhin, E. N. Kalaidin, S. Kalliadasis, and S. Yu. Vlaskin, Phys. Fluids **19**, 114104 (2007).
[11] E. A. Demekhin, E. N. Kalaidin, S. Kalliadasis, and S. Yu. Vlaskin, Phys. Rev. E **82**, 036322 (2010).
[12] M. Pradas, D. Tseluiko, and S. Kalliadasis, Phys. Fluids **23**, 044104 (2011).
[13] M. Pradas, S. Kalliadasis, and D. Tseluiko, IMA J. Appl. Math. **77**, 408 (2012).
[14] D. Tseluiko, and S. Kalliadasis, IMA J. Appl. Math. **79**, 274 (2014).
[15] R. M. Roberts, and H.-C. Chang, Chem. Eng. Sci. **55**, 1127 (2000).
[16] R. Mathie, H. Nakamura, and C. N. Markides, Int. J. Heat Mass Transfer **56**, 819 (2013).
[17] C. Yih, Phys. Fluids **6**, 321 (1963).
[18] R. Kelly, D. Goussis, S. Lin, and F. Hsu, Phys. Fluids A **1**, 819 (1989).
[19] H.-C. Chang, Annu. Rev. Fluid Mech. **26**, 103 (1994).
[20] J. Liu and J. Gollub, Phys. Fluids **6**, 1702 (1994).
[21] S. Kalliadasis, C. Ruyer-Quil, B. Scheid, and M. Velarde, *Falling Liquid Films*, Applied Mathematical Sciences Vol. 176 (Springer-Verlag, London, 2012).
[22] S. Kalliadasis, A. Kiyashko, and E. A. Demekhin, J. Fluid Mech. **475**, 377 (2003).
[23] S. Kalliadasis, E. A. Demekhin, C. Ruyer-Quil, and M. G. Velarde, J. Fluid Mech. **492**, 303 (2003).
[24] P. M. J. Trevelyan and S. Kalliadasis, J. Eng. Math. **50**, 177 (2004).
[25] B. Scheid, C. Ruyer-Quil, S. Kalliadasis, M. G. Velarde, and R. K. Zeytounian, J. Fluid Mech. **538**, 223 (2005).
[26] P. M. J. Trevelyan, B. Scheid, C. Ruyer-Quil, and S. Kalliadasis, J. Fluid Mech. **592**, 295 (2007).
[27] P. M. J. Trevelyan and S. Kalliadasis, Phys. Fluids **16**, 3191 (2004).
[28] P. M. J. Trevelyan and S. Kalliadasis, Phys. Fluids **16**, 3209 (2004).
[29] P. M. J. Trevelyan, A. Pereira, and S. Kalliadasis, Math. Model. Nat. Phenom. **7**, 99 (2012).
[30] A. Pereira and S. Kalliadasis, Phys. Rev. E **78**, 036312 (2008).
[31] C. Duprat, C. Ruyer-Quil, S. Kalliadasis, and F. Giorgiutti-Dauphiné, Phys. Rev. Lett. **98**, 244502 (2007).
[32] C. Ruyer-Quil, P. M. J. Treveleyan, F. Giorgiutti-Dauphiné, C. Duprat, and S. Kalliadasis, J. Fluid Mech. **603**, 431 (2008).
[33] C. Duprat, F. Giorgiutti-Dauphiné, D. Tseluiko, S. Saprykin, and S. Kalliadasis, Phys. Rev. Lett. **103**, 234501 (2009).
[34] D. Tseluiko, S. Saprykin, C. Duprat, F. Giorgiutti-Dauphiné, and S. Kalliadasis, Physica D **239**, 2000 (2010).
[35] C. Ruyer-Quil and S. Kalliadasis, Phys. Rev. E **85**, 046302 (2012).
[36] B. Scheid, C. Ruyer-Quil, and P. Manneville, J. Fluid Mech. **562**, 183 (2006).
[37] F. Denner, A. Charogiannis, M. Pradas, B. van Wachem, C. N. Markides, and S. Kalliadasis (unpublished).
[38] E. Doro and C. Aidun, J. Fluid Mech. **726**, 261 (2013).
[39] W. Rohlfs and B. Scheid, J. Fluid Mech. **763**, 322 (2015).
[40] D. Maron, N. Brauner, and G. Hewitt, Int. Commun. Heat Mass Transfer **16**, 655 (1989).
[41] D. Gao, N. Morley, and V. Dhir, J. Comput. Phys. **192**, 624 (2003).
[42] H. Yu, T. Gambaryan-Roisman, and P. Stephan, J. Heat Transfer **135**, 101010 (2013).
[43] C. Albert, H. Marschall, and D. Bothe, Int. J. Heat Mass Transfer **69**, 343 (2014).
[44] S. Chakraborty, P.-K. Nguyen, C. Ruyer-Quil, and V. Bontozoglou, J. Fluid Mech. **745**, 564 (2014).
[45] J. Liu, J. Paul, and J. Gollub, J. Fluid Mech. **250**, 69 (1993).
[46] T. Nosoko and A. Miyara, Phys. Fluids **16**, 1118 (2004).
[47] F. Denner and B. van Wachem, Numer. Heat Transfer, Part B **65**, 218 (2014).
[48] F. Denner and B. van Wachem, J. Comput. Phys. **279**, 127 (2014).

[49] F. Denner and B. van Wachem, J. Comput. Phys. **285**, 24 (2015).
[50] V. Levich and V. Krylov, Annu. Rev. Fluid Mech. **1**, 293 (1969).
[51] W. Nusselt, VDI Zeitschrift (VDI Z.) **60**, 541 (1916).
[52] V. Shkadov, Izv. Akad. Nauk SSSR, Mekh. Zhidk. Gaza **12**, 63 (1977).
[53] T. Salamon, R. Armstrong, and R. Brown, Phys. Fluids **6**, 2202 (1994).
[54] T. Ooshida, Phys. Fluids **11**, 3247 (1999).
[55] C. Ruyer-Quil and P. Manneville, Eur. Phys. J. B **6**, 277 (1998).
[56] C. Ruyer-Quil and P. Manneville, Eur. Phys. J. B **15**, 357 (2000).
[57] C. Ruyer-Quil and P. Manneville, Phys. Fluids **14**, 170 (2002).
[58] R. Clift, J. Grace, and M. Weber, *Bubbles, Drops and Particles* (Academic, New York, 1978), p. 379.
[59] D. Bhaga and M. Weber, J. Fluid Mech. **105**, 61 (1981).
[60] J. Eggers and E. Villermaux, Rep. Prog. Phys. **71**, 036601 (2008).
[61] J. Shinjo and A. Umemura, Int. J. Multiphase Flow **36**, 513 (2010).
[62] S. Navarro-Martinez, Int. J. Multiphase Flow **63**, 11 (2014).
[63] H.-C. Chang, E. Demekhin, and E. Kalaidin, J. Fluid Mech. **294**, 123 (1995).
[64] M. K. R. Panga and V. Balakotaiah, Phys. Rev. Lett. **90**, 154501 (2003).
[65] M. K. R. Panga, R. R. Mudunuri, and V. Balakotaiah, Phys. Rev. E **71**, 036310 (2005).
[66] R. Dembo, S. Eisenstat, and T. Steihaug, SIAM J. Numer. Anal. **19**, 400 (1982).
[67] C. Hirt and B. Nichols, J. Comput. Phys. **39**, 201 (1981).
[68] O. Ubbink and R. Issa, J. Comput. Phys. **153**, 26 (1999).
[69] J. Brackbill, D. Kothe, and C. Zemach, J. Comput. Phys. **100**, 335 (1992).
[70] S. Cummins, M. Francois, and D. Kothe, Comput. Struct. **83**, 425 (2005).
[71] F. Denner and B. van Wachem, Int. J. Multiphase Flow **54**, 61 (2013).
[72] F. Denner, D. van der Heul, G. Oud, M. Villar, A. da Silveira Neto, and B. van Wachem, Int. J. Multiphase Flow **61**, 37 (2014).
[73] F. Denner, Balanced-force two-phase flow modelling on unstructured and adaptive meshes, Ph.D. thesis, Imperial College London, 2013, http://hdl.handle.net/10044/1/28101.
[74] F. Denner and B. van Wachem, J. Comput. Phys. **298**, 466 (2015).
[75] C. Albert, H. Raach, and D. Bothe, Int. J. Multiphase Flow **43**, 66 (2012).
[76] M. Pradas, S. Kalliadasis, P.-K. Nguyen, and V. Bontozoglou, J. Fluid Mech. **716**, R2 (2013).
[77] S. Joo, S. Davis, and S. Bankoff, Phys. Fluids A **3**, 231 (1991).
[78] E. Doro, Computational modeling of falling liquid film free surface evaporation, Ph.D. thesis, Georgia Institute of Technology, 2012 .
[79] H. Lamb, *Hydrodynamics*, 6th ed. (Cambridge University Press, Cambridge, 1932).
[80] J. Lighthill, *Waves in Fluids* (Cambridge University Press, Cambridge, 1978), p. 504.
[81] V. Levich, *Physicochemical Hydrodynamics* (Prentice-Hall, Englewood Cliffs, NJ, 1962).
[82] J. C. Earnshaw, and C. J. Hughes, Langmuir **7**, 2419 (1991).
[83] P. LeBlond and L. Mysak, *Waves in the Ocean* (Elsevier, New York, 1978).
[84] See http://dx.doi.org/10.5281/zenodo.46738.